

Scatterless interferences: Delay of laminar-to-turbulent flow transition by a lattice of subsurface phonons

Mahmoud I. Hussein,^{1,2,*} David Roca,³ Adam R. Harris,¹ and Armin Kianfar¹

¹*Smead Department of Aerospace Engineering Sciences,
University of Colorado, Boulder, Colorado 80303*

²*Department of Physics, University of Colorado, Boulder, Colorado 80302*

³*Centre Internacional de Mètodes Numèrics en Enginyeria (CIMNE),
Universitat Politècnica de Catalunya, Barcelona 08034, Spain*

Turbulent flows in boundary layers generate significantly higher surface friction drag compared to laminar flows. Avoidance or delay of laminar-to-turbulent flow transition is therefore critical for efficient operation of air vehicles and water vessels. Here we present a passive phonons-based solution that is based on engineered intervention with the unstable flow fluctuations that trigger the transition. The intervention is introduced by a tailored frequency- and wavevector-dependent interaction between the flow and the bounding surface. The surface is homogenous and smooth with all the engineered constituents buried in the subsurface. The subsurface configuration comprises a wall-parallel lattice of wall-normal phononic structural units. Each discrete phononic subsurface unit is designed to respond to the flow in a negative phase as to inhibit the flow instabilities at the point of contact. The collective effect of the lattice formation of these units, in turn, offers a form of interferences that causes the kinetic energy of the flow instabilities to decay downstream to the location of the intervention, thus delaying the transition. This concept presents a new paradigm for the design of aircrafts and ships beyond the prevailing paradigm of streamlined shaping of the surfaces.

The interaction of a flowing fluid with a surface is a dynamical process that lies at the heart of a wide range of both natural and artificial systems. Two most consequential examples are the flow over an aircraft wing or around the hull of a ship. The nature of the fluid-structure interaction in these cases dictates the intensity of skin-friction drag, the location of onset of laminar-to-turbulent flow transition, and the possibility of flow separation—all with far-reaching implications on the overall performance of the vehicle [1, 2]. Skin friction drag in particular has profound economic and environmental costs because it directly affects the fuel efficiency. Effective intervention that delays flow transition is thus critical because wall-bounded turbulent flows generate significantly higher surface friction drag compared to laminar flows. Flow separation, as a contrasting scenario, is key to overall aerodynamic/hydrodynamic stability, form drag, vehicle maneuverability, and applications that require turbulent mixing. Similar considerations for fluid-structure interaction are applicable to other problems, such as land vehicles, wind turbines, and long-range pipelines, to name a few.

Laminar-to-turbulent transition in walled-bounded flows has been investigated extensively in the past, leading to a rich build-up of knowledge on how transition occurs across various flow regimes [3]. A “natural” form of transition is associated with the growth in amplitude of infinitesimal fluctuations (also referred to as perturbations or disturbances [4]) representing unstable propagating modes inherent in the flow. If left without intervention, these modes advance to nonlinear growth,

secondary transition mechanisms, flow structure breakdown, and finally fully developed turbulent flow [3]. A dominant primary mode in air or water channel flows or boundary layers is known as Tollmien-Schlichting (T-S) waves [5, 6]. These unstable waves, which travel with the mean flow, have a vortical nature and grow over an identifiable narrow band of frequencies that can be predicted with linear stability analysis [7, 8]. Although T-S waves are not always the mechanism directly responsible for transition, particularly under realistic flight conditions, much research has been devoted to their understanding [9] due to their fundamental nature, and because they serve as a platform for development of new technologies for laminar flow control involving more complex types of instabilities.

Numerous research approaches have been proposed in the last couple of decades aimed at passively mitigating the undesirable effects of fluid-structure interactions. These include installation of riblets over the surface [10, 11], creation of artificial surface roughness [12, 13], drilling of holes to form a porous surface [14, 15], or coating the surface with a compliant (low stiffness) material [16–22]. None of these approaches, however, synchronize with the frequency, phase, and wavevector characteristics of the flow instabilities, and are therefore limited in their effectiveness. An ideal intervention requires a tailored solution, with mechanistic precision, to create a passive and responsive control stimulus that accounts for the dynamical properties of the underlying flow transition mechanisms. In 2015, the general concept of flow control by subsurface phonons has been introduced as an approach capable of achieving this level of precise wave-synchronized control of flow instabilities [23]. A phononic subsurface (PSub) com-

* mih@colorado.edu

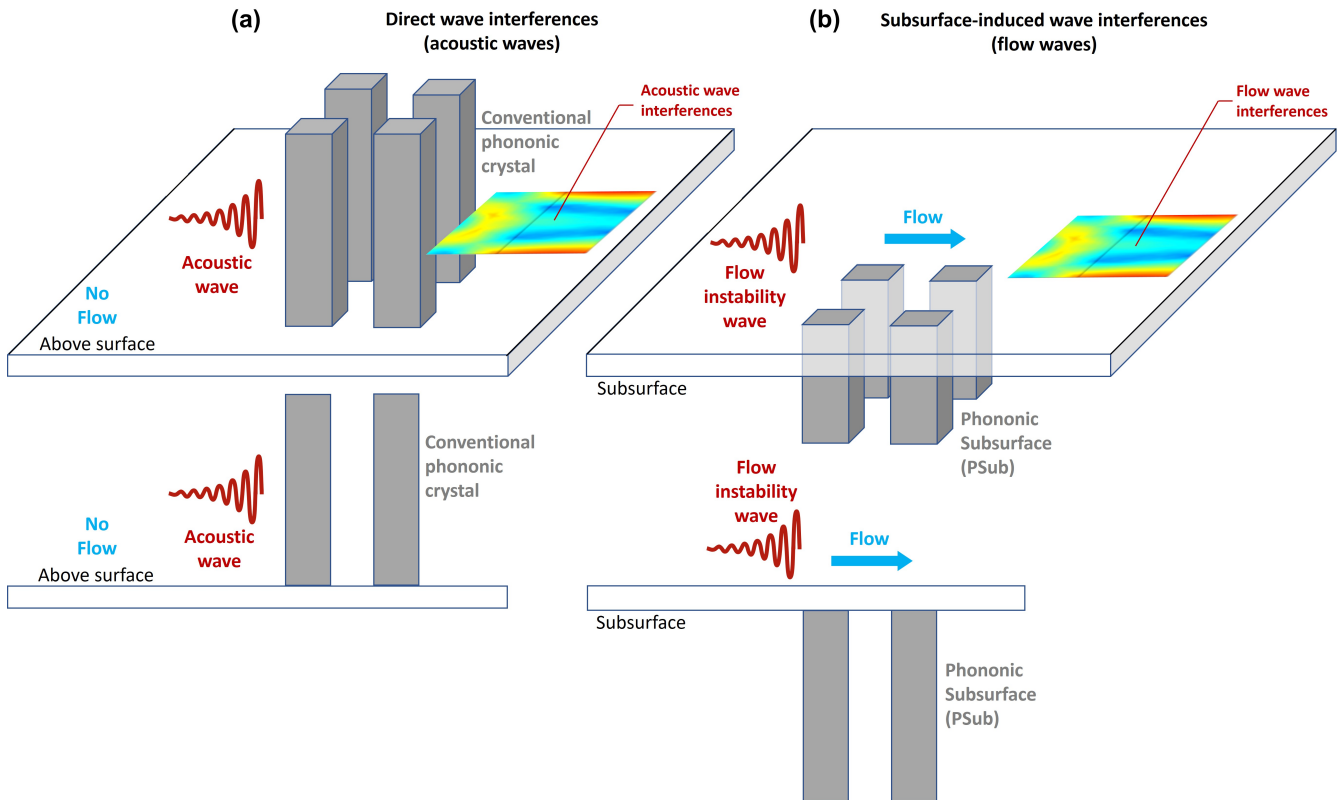


Figure 1. **Illustration of scatterless interferences:** (a) Classical scattering of acoustic waves by a lattice of elastic objects, where the interfering waves and the objects are in the same space. (b) Scatterless interferences of flow fluctuation waves by a lattice of PSubs, where the waves and the PSubs are not in the same space.

prises a synthetically designed architected material affixed beneath [24] the surface exposed to the flow (e.g., of a wing or vehicle body). The function of the PSub is to manipulate small-amplitude vibrations on the surface, and by extension the flow fluctuations near the wall that are responsible for transition. PSubs may be designed to passively respond to the flow instabilities in an out-of-phase manner, creating stabilization, or in an in-phase manner, creating destabilization—either function is realized by design. In past computational investigations, a PSub has been applied as a solitary unit [23, 25–28] or as a contiguous layout of units distributed along the streamwise direction [29, 30].

Despite the rapid progress of research on flow control by subsurface phonons, critical aspects remain to be addressed for the general concept to reach its potential. Two key limitations of previous demonstrations are that the PSub effect is not effective downstream to the PSub location, and that it is applicable only on unidirectional instability waves. The former must be resolved to enable transition delay, and the latter is significant for real-world flow control. While the downstream control objective was addressed with a “multiple-input-multiple-output” PSub configuration, offering a remarkable explicit display of transition delay [25], that approach is inherently limited to unidirectional instabilities because it dictates that a single PSub must interact with more

than one flow point requiring a phased relation to be tuned specifically along a certain direction. Furthermore, the fixed distance between the input/output points limits the approach to a narrow band of fluctuation wavenumbers. Schmidt et al. [28] explored the concept from an alternative angle: rather than engage with subsurface phonons to inhibit the fluctuation production mechanisms (as done in all previous PSub studies), they designed their PSub based on pass-band motion to absorb and trap the fluctuation energy by resorting to actively controlled time-varying material properties. This approach enhances the energy transfer from the mean flow to the instabilities, rather than reduces it [26]. When more energy is drawn from the mean flow, this energy will accumulate in the subsurface structure requiring its dissipation as heat.

In this work, we present the concept of a *lattice of PSubs* comprising a collection of individual PSub units laid out following a square or hexagonal lattice symmetry [31]. Similar to acoustic or elastic waves propagating around or through a lattice of scatterers (see Fig. 1a), we design our configuration on the basis of a rigorous Bloch wave analysis where the field variable is the flow fluctuations. Yet, in our system there are no scatterers. In contrast to classical scattering problems where the interfering waves and the scattering objects are in the same space, the flow instability waves interfere

as a result of the local influence of each PSub on the fluctuation velocity components. Here we recall that the PSub is beneath the space of the flow (see Fig. 1b). After developing Bloch’s theorem for this unique problem, we demonstrate by direct numerical simulations of the coupled fluid-Psub lattice system sustained downstream reduction in the fluctuations kinetic energy, which indicates a delay in laminar-to-turbulent transition. Moreover, as dictated by the PSub lattice symmetry, this approach is immune to any changes in the direction of propagation of the instability waves and may be tuned to accommodate a wide range of wavenumbers along each direction—similar to the classical acoustic Bragg scattering problem which we also demonstrate to provide a direct analogy and comparison.

Results

We form our lattice of Psubs using identical PSub units, all installed in a channel model. We select a channel flow problem for simplicity, but all the underlying concepts are readily applicable to boundary layer flows. The Psub design used in this investigation is shown in Fig. 2a. It consists of an elastic rod, composed of five unit cells, with each unit cell accomodating a local resonator (which in practice may be realized as a cantilevered pillar). The dispersion curves and the amplitude and phase frequency-response characteristics for this nominal PSub configuration is shown in Fig. 2b. The product of the amplitude and phase yields a performance metric which provides an *a priori* prediction of the beahvior of the PSub once passively engaged with the flow—this quantity is also plotted in Fig. 2b.

Figure 3 shows the results of applying Bloch analysis over a unit cell comprising the flow interacting with the PSub in three configurations, a full-span PSub, and the square and hexagonal lattice arrangements [see schematics (b), (c) and (d) in Fig. 3]. The PSub interaction with the flow has been accounted for through a frequency-dependent complex-valued admittance, denoted by Y in Fig. 3(a). The admittance is obtained, for a given frequency, from the solution of the PSub system of equations [25] and it is closely related to the performance metric. We use this function alongside transpiration boundary conditions to find the most unstable eigenvalue—and associated eigenmode—from the standard Orr-Sommerfeld equations modified to accommodate the periodicity imposed by the application of Bloch’s theorem in terms of the T-S wave’s wavenumber, which corresponds to the eigenvalue. The mathematical details of the formulation can be found in the Supplementary Material. As a result of this analysis, the dispersion curves corresponding to the unstable flow mode in Fig. 3(a) have been obtained. These results are complemented by the rate of production of perturbation kinetic energy (PKE)—denoted by P_r in Fig. 3—obtained from the Bloch analysis. These have been computed from the eigenmodes associated with the unstable eigenvalues, normalized by the average PKE computed for the rigid

case (refer to Supplementary Materials for details). Results for both weak destabilizing and stabilizing cases, at frequencies of 1539.5 Hz and 1555 Hz respectively, have been averaged over a flow domain close to the PSub wall, in particular along 10% of the channel’s half height. Contour plots showing the P_r spanwise distribution over three unit cells (in the streamwise direction) are given in Fig. 3(b) to (d) for the full-span and for each of the lattice configurations. The average P_r values over a spanwise period are shown in the last row of Fig. 3(b) to (d) to summarize the results. The different cases are compared with the results for the rigid case, to show the spatial stabilizing/destabilizing effects when the flow interacts with each PSub patch.

The ultimate test for any flow control approach is through high-fidelity simulations, particularly direct numerical simulations (DNS) of the Navier-Stokes equations, as these resolve the high spatial and temporal frequencies of the flow fluctuations—which are central to the transition mechanism. We execute simulations in a three-dimensional (3D) computational domain and retain all nonlinear terms. In Fig. 4 we present DNS results for the two lattice configurations, and also show the results of an analogous acoustic scattering simulation for comparison. The coupled fluid-structure simulations were run at $Re = 7500$ with a 1555 Hz unstable T-S wave input at the left end of the channel. See the Models and Methods sections for more details on the model and simulation parameters and numerical techniques used. The results in Figs. 4b and 4c show a sustained reduction in the PKE downstream of the PSub lattice, with a slightly stronger effect by the hexagonal arrangement compared to the square arrangement.

Discussion

The performance metric for the designed PSub unit shown in Fig. 2b shows that the unstable wave frequency of 1555 Hz falls at a negative value, indicative of a stabilization effect. While the surrounding negative region is relatively narrow—since it is associated with a given structural resonance of the finite PSub structure, future work will explore strategies to broaden the frequency range of operation.

Results from the Bloch analysis show a correlation between the dispersion curves (in Fig. 3) and the PSub performance metric (in Fig. 2). It is observed that the intensity of the T-S wave’s instability—in this case given by the imaginary wavenumber—rapidly grows in the vicinity of the resonance frequency, which helps enhance the stabilizing/destabilizing effects. Furthermore, the rate of production of PKE within the PSub region consistently increases in the destabilizing case and decreases—even reaching negative values—in the stabilizing case, in agreement with the stand-alone performance metric predictions (see Fig. 3(b) to (d)). Interestingly, the P_r also exhibits an opposite effect upon leaving the PSub, which is in accordance with what we observe in the fluid-structure interaction (FSI) simulations (see, for instance, how the PKE slightly increases in Figs. 4(b) and (c) each time

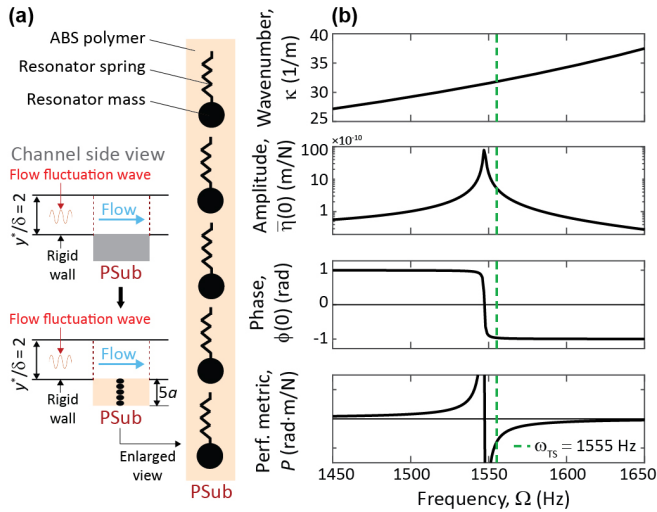


Figure 2. PSub design and its dispersion and vibration response characteristics: (a) Schematic of locally-resonant elastic metamaterial-based PSub utilized in this study. The length of the unit cell is $a_{\text{PSub}} = 1$ cm yielding a total PSub length of 5 cm. Each PSub is installed in the flow subsurface with its top face directly exposed to the flow. Flow instabilities, e.g. T-S waves, will continuously excite the PSub at the top edge and the PSub, in turn, will respond at the same point. Depending on the frequency, the PSub will respond according to its dynamical characteristics. Close to an anti-resonance or a resonance, the PSub motion will respectively impede or enhance the energy extraction from the mean flow into the fluctuation field [26]. This passive process will repeat and cause sustained control of incoming instability waves near the wall at the location of the PSub. (b) Four key plots that characterize the PSubs dynamics. From top to bottom, the following are shown: dispersion curves for PSub unit cell, steady-state vibration amplitude and phase response of the PSub top edge when excited at the same location, and performance metric obtained by multiplying the amplitude by the phase. All plots are obtained by analyzing a stand-alone finite-element model of the PSub.

the flow leaves a PSub unit behind despite being stabilizing cases). This analysis also shows how the full-span case exhibits a stronger response than both lattice configurations, which demonstrates that spanwise interactions can affect the flow instabilities downstream, as demonstrated by the full-scale FSI simulations results. While both square and hexagonal PSub lattices are effective in sustaining downstream stabilization, both the Bloch analysis and simulations indicate that the hexagonal configuration is slightly superior—its PKE slope in Fig. 4c is $\theta = 4.6^\circ$ compared to $\theta = 4.4^\circ$ for the square lattice. Upon further design optimization of both the PSub unit and the lattice configuration, stronger downstream reductions in PKE are attainable. It is clearly observed that both flow fluctuations “scatterless” interferences are nearly identical to the interferences triggered by acoustic scattering.

In conclusion, we have demonstrated that by engineering the phonon properties of the subsurface, which

could very well be concealed, it is possible to almost completely execute full command of the very nature of the fluid-structure interaction. Such intervention, which is fully passive, offers precise mechanistic control of the behavior of wall-bounded flows. Our findings demonstrate that the principles of Bloch analysis, traditionally applied to acoustic and elastic waves, can be effectively translated into the realm of flow control through the implementation of PSubs. By leveraging locally resonant metamaterial-based phononic subsurfaces, we have shown that it is possible to manipulate flow instabilities in a manner analogous to wave propagation in periodic acoustic and elastic media. This novel approach enables passive control of phenomena such as transition to turbulence, with lattice arrangements of PSubs facilitating attenuation of T-S waves’ instabilities downstream, while also being robust to variations in wavenumber and direction of propagation. With the advent of concepts from phonon engineering and metamaterials, the prospects of future improvements of the performance is highly accessible. It is conceivable, for example, that with architected materials, a fully laminar boundary layer around an airplane may be attained in the near future. Such outcome would drastically improve fuel efficiency. Potentially, the Psub lattices may be designed to simultaneously inhibit noise emission as well, which would bring about the added advantage of passenger comfort and reduced noise pollution.

Models and Methods

Governed by the 3D Navier-Stokes equations, we run a series of direct numerical simulations for incompressible channel flows. The velocity vector solution is expressed as $\mathbf{u}(x, y, z, t) = (u, v, w)$ with components in the streamwise x , wall-normal y , and the spanwise z directions, respectively, where t denotes time. The DNS is run for a Reynolds number of $Re = \rho_f U_c \delta / \mu_f = 7500$ based on a centerline velocity $U_c = 17.12$ m/s and a half-height of the channel $\delta = 4.38 \times 10^{-4}$ m. Liquid water is considered with a density of $\rho_f = 1000$ kg/m³ and dynamic viscosity of $\mu_f = 1 \times 10^{-3}$ kg/ms. All subsequent quantities, unless mentioned explicitly, are normalized by the channel’s velocity U_c and length δ scales. The channel size is $0 \leq x \leq 30$, $0 \leq y \leq 2$, and $0 \leq z \leq 2\pi$ for the streamwise, wall-normal, and spanwise directions, respectively. At the inlet of the channel, a fully developed Poiseuille flow is superimposed with an unstable T-S mode obtained from linear hydrodynamic stability analysis governed by the Orr-Sommerfeld equation [32, 33] and solved for the same Re . The least-damped eigensolution is selected which has complex wavenumber $\alpha = 1.0004 - i0.006171$ and real non-dimensional frequency $\omega_{\text{TS}} = 0.250$. Following dimensional analysis, the frequency of the corresponding T-S wave is $\Omega_{\text{TS}} = \omega_{\text{TS}} U_c / 2\pi\delta = 1555$ Hz. To ensure outgoing wave motion on the other side of the channel, the disturbances are smoothly brought to zero by attaching a non-reflective buffer region at

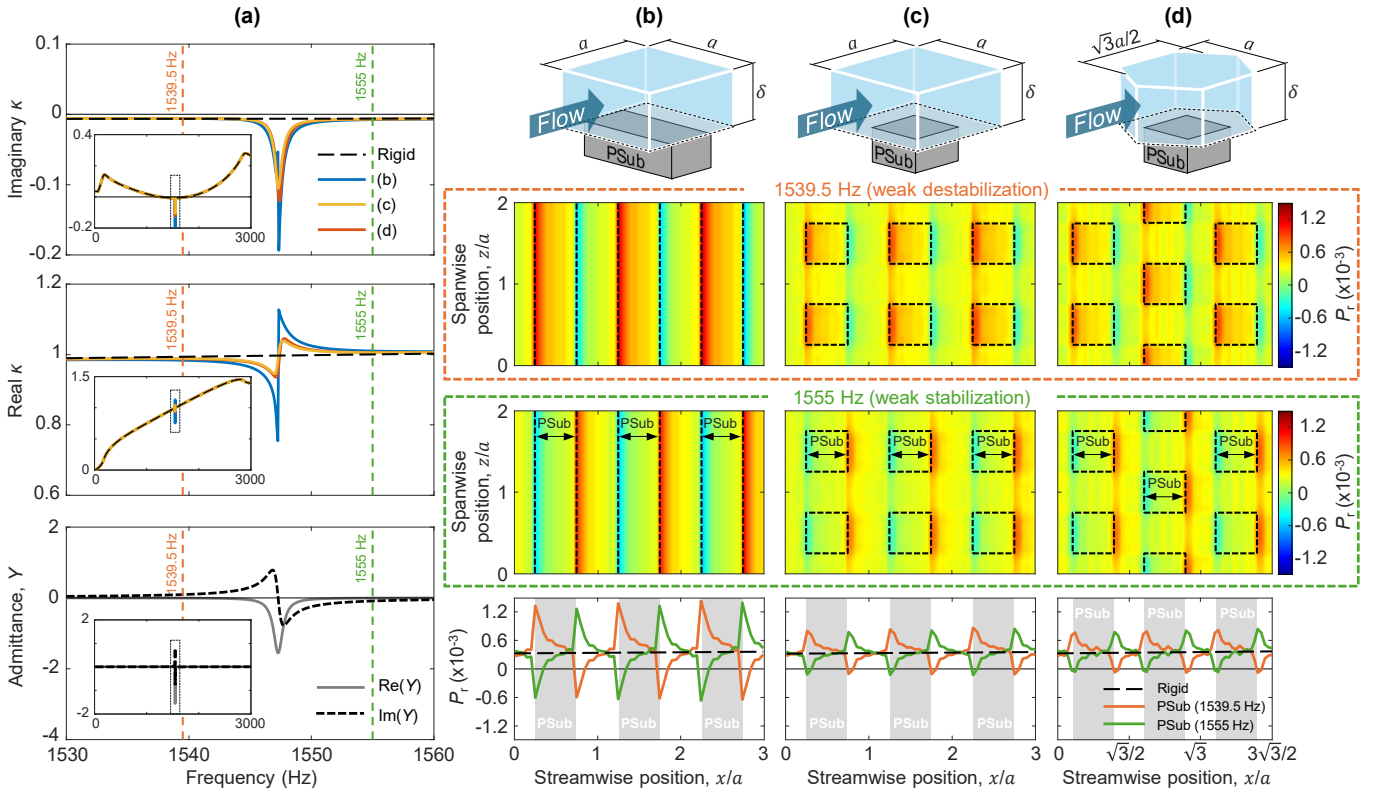


Figure 3. (a) **Dispersion curves for selected unstable flow mode in the presence of a PSub lattice.** The first and second rows correspond to the imaginary and real components of the wavenumber κ for the rigid cases and the PSub cases in the full-span, square-lattice and hexagonal-lattice configurations [depicted by the (b), (c) and (d) unit cell schematics, respectively]. The third row shows the real and imaginary components of the PSub’s admittance Y at different frequencies. The dashed vertical lines indicate the frequencies for which the average modal perturbation kinetic energy (PKE) production rate, P_r , distributions on the right plots have been obtained. Results for each frequency are depicted in their corresponding panel. The first panel (in orange) shows a weak destabilizing case (at a frequency of 1539.5 Hz) and the second panel (in light green) is for a weak stabilizing case (at a frequency of 1555 Hz). The curves below the panels correspond to the averaged production rate evolution obtained for both the weak destabilizing and stabilizing cases compared to that of the rigid case. As a reference, the average has been evaluated in the vicinity of the PSub wall (in the range of 10% of half of the channel’s height), and all the modal amplitudes have been normalized to make them coincide with that of the rigid case at the left edge of the first unit cell.

the outlet [34–36]. Periodic boundary conditions are applied in the spanwise direction. At the top and bottom walls no-slip, no-penetration boundary conditions are applied, except within the control region from x_s to x_e in the streamwise direction where the rigid wall is replaced by a PSub, or a lattice of PSubs, at the bottom wall. Within the control region, the fluid-structure coupling is enforced by means of transpiration boundary conditions [23, 37, 38] (see Supplementary Material). These boundary conditions are valid if the PSub motion is only in the wall-normal direction and $\eta \ll \delta$ where η is the wall-normal displacement of the PSub. Hence, throughout DNS the roughness Reynolds number is monitored and maintained below 25 [39].

Each PSub unit is modeled as a finite linear elastic metamaterial consisting of 5 rod unit cells with one local mass-spring resonator in the center of the unit cell [26, 30]. The PSub is free to deform at the edge interfacing with the flow (top) and is fixed at the other end (bottom). Each individual PSub is allowed

to deform independently from the adjacent rigid wall and from the motion of neighboring PSubs; its top surface deformation takes a uniform profile across the fluid-PSub interface region [30]. The length of the unit cell along the wall-normal direction is $L_{UC} = 1$ cm (i.e., total PSub length is 5 cm). The resonator frequency are set to $\Omega_{res} = 2000$ Hz by tuning the resonators point masses to be ten times heavier than the total mass of the unit-cell base ($m_{res} = 10 \times \rho L_{UC}$), where ρ is the base material density. Hence, the stiffness of the resonator spring is $k_{res} = m_{res}(2\pi f_{res})^2$. The base is composed of ABS polymer with density of $\rho = 1200$ kg/m³ and Young’s modulus of $E = 3$ GPa. Material damping is modeled as viscous proportional damping with constants $q_1 = 0$ and $q_2 = 6 \times 10^{-8}$ [30].

The Navier-Stokes equations are integrated using a time-splitting scheme [34–36] on a staggered structured grid system. A two-node iso-parametric finite-element model is used for determining the PSub nodal axial displacements, velocities, and accelerations [40] where

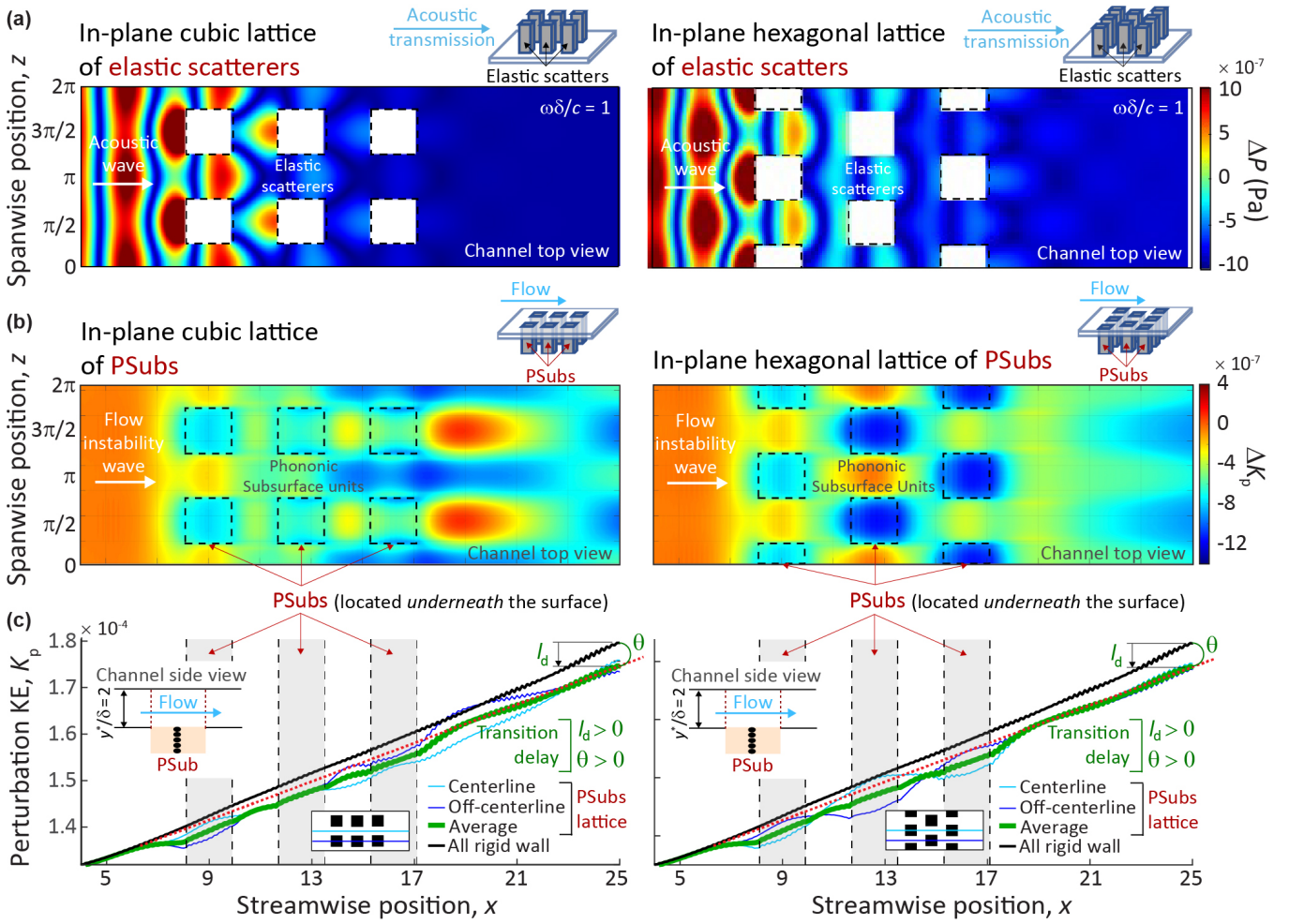


Figure 4. **Demonstration of scatterless interferences by DNS:** (a) Acoustic wave propagation in a space covered by a lattice of elastic scatterers, considering square symmetry (left) and hexagonal symmetry (right). (b) Time-averaged flow PKE as a function of the streamwise and spanwise directions for flow in a channel with PSubs laid out following both symmetries. (c) Time- and spanwise-averaged PKE as a function of the streamwise position. The results in (b) and (c) indicate interference patterns, even though the surface is flat and there are no objects in the flow space. These interferences stem for the collective action of the local effect by each PSub. Figure 4(c) shows time-averaged PKE on and off the centerline of the channel, reflecting the effects of the different symmetries of the square and hexagonal lattices. The time- and spanwise-averaged PKE is shown in dark green, where the angle θ at the end of the channel indicates a decrease in the slope of PKE compared to the rigid case, and hence transition delay downstream of the PSub lattice. The angle is measured as $\theta = 4.4^\circ$ and $\theta = 4.6^\circ$ for the square and hexagonal cases, respectively, indicating the transition is delayed further by the hexagonal PSubs lattice.

time integration is implemented simultaneously with the flow simulation using an implicit Newmark algorithm [41]. Since the equations for the fluid and the PSub are inverted separately in the coupled simulations, a conventional serial staggered scheme [42] is implemented to couple the two sets of time integration. More details on the computational models and numerical schemes used are detailed in Refs. [26, 30]. The relative geometric dimensions of the PSubs forming each of the square and hexagonal lattices are to scale as shown in Fig. 4, with more information available in the Supplemental Materials document.

Acknowledgments

This work utilized the Summit supercomputer, which is supported by the National Science Foundation (awards ACI-1532235 and ACI-1532236), the University of Colorado Boulder, and Colorado State University. The Summit supercomputer is a joint effort of the University of Colorado Boulder and Colorado State University. This work also utilized the Alpine high performance computing resource at the University of Colorado Boulder. Alpine is jointly funded by the University of Colorado Boulder, the University of Colorado Anschutz, and Colorado State University and with support from NSF grants OAC-2201538 and OAC-2322260.

- [1] L. Prandtl, “Modern developments in flow control,” in *Proc. 3rd Int. Congress of Mathematicians, Heidelberg, Germany, 8–13 August 1904, Leipzig, Germany: Druck und Verlag von B. G. Teubner*, pp. 484–491, 1904.
- [2] M. Gad-el Hak, A. Pollard, and J.-P. Bonnet, *Flow control: Fundamentals and practices*, vol. 53. Springer Science & Business Media, 2003.
- [3] M. V. Morkovin, “On the many faces of transition,” in *Viscous Drag Reduction: Proceedings of the Symposium on Viscous Drag Reduction held at the LTV Research Center, Dallas, Texas, September 24 and 25, 1968*, pp. 1–31, Springer, 1969.
- [4] These terms are used interchangeably in this article.
- [5] W. Tollmien, “Über die entstehung der turbulenz. 1. mitteilung,” *Nachrichten von der Gesellschaft der Wissenschaften zu Göttingen, Mathematisch-Physikalische Klasse*, vol. 1929, pp. 21–44, 1928.
- [6] H. Schlichting, “Zur entstehung der turbulenz bei der plattenströmung,” *Nachrichten von der Gesellschaft der Wissenschaften zu Göttingen, Mathematisch-Physikalische Klasse*, vol. 1933, pp. 181–208, 1933.
- [7] G. B. Schubauer and H. K. Skramstad, “Laminar boundary-layer oscillations and stability of laminar flow,” *Journal of the Aeronautical Sciences*, vol. 14, no. 2, pp. 69–78, 1947.
- [8] L. M. Mack, “Boundary-layer linear stability theory,” *Agard rep*, vol. 709, 1984.
- [9] P. Carpenter and A. Garrad, “The hydrodynamic stability of flow over kramer-type compliant surfaces. part 1. tollmien-schlichting instabilities,” *Journal of Fluid Mechanics*, vol. 155, pp. 465–510, 1985.
- [10] M. J. Walsh and L. M. Weinstein, “Drag and heat transfer on surfaces with small longitudinal fins,” in *11th Fluid and Plasma Dynamics Conference, Seattle, Washington, USA, July 11-12, 1978*.
- [11] R. García-Mayoral and J. Jiménez, “Drag reduction by riblets,” *Philosophical Transactions of the Royal Society A*, vol. 369, pp. 1412–1427, 2011.
- [12] C. Cossu and L. Brandt, “Stabilization of Tollmien–Schlichting waves by finite amplitude optimal streaks in the blasius boundary layer,” *Physics of Fluids*, vol. 14, pp. L57–L60, 2002.
- [13] J. H. M. Fransson, L. Brandt, A. Talamelli, and C. Cossu, “Experimental study of the stabilization of Tollmien–Schlichting waves by finite amplitude streaks,” *Physics of Fluids*, vol. 17, p. 054110, 2005.
- [14] A. V. Fedorov, N. D. Malmuth, A. Rasheed, and H. G. Hornung, “Stabilization of hypersonic boundary layers by porous coatings,” *AIAA journal*, vol. 39, no. 4, pp. 605–610, 2001.
- [15] N. Abderrahaman-Elena and R. García-Mayoral, “Analysis of anisotropically permeable surfaces for turbulent drag reduction,” *Physical Review Fluids*, vol. 2, p. 114609, 2017.
- [16] M. O. Kramer, “Boundary layer stabilization by distributed damping,” *Naval Engineers Journal*, vol. 74, no. 2, pp. 341–348, 1962.
- [17] T. B. Benjamin, “Effects of a flexible boundary on hydrodynamic instability,” *Journal of Fluid Mechanics*, vol. 9, pp. 513–532, 1960.
- [18] D. M. Bushnell, J. N. Hefner, and R. L. Ash, “Effect of compliant wall motion on turbulent boundary layers,” *Physics of Fluids*, vol. 20, pp. S31–S48, Oct. 1977.
- [19] M. Gad-El-Hak, R. F. Blackwelder, and J. J. Riley, “On the interaction of compliant coatings with boundary-layer flows,” *Journal of Fluid Mechanics*, vol. 140, p. 257–280, 1984.
- [20] P. W. Carpenter and A. D. Garrad, “The hydrodynamic stability of flow over Kramer-type compliant surfaces. part 1. Tollmien–Schlichting instabilities,” *Journal of Fluid Mechanics*, vol. 155, p. 465–510, 1985.
- [21] A. D. Lucey and P. W. Carpenter, “Boundary layer instability over compliant walls: Comparison between theory and experiment,” *Physics of Fluids*, vol. 7, pp. 2355–2363, 1995.
- [22] C. Davies and P. W. Carpenter, “Numerical simulation of the evolution of Tollmien–Schlichting waves over finite compliant panels,” *Journal of Fluid Mechanics*, vol. 335, pp. 361–392, 1997.
- [23] M. I. Hussein, S. Biringen, O. R. Bilal, and A. Kucala, “Flow stabilization by subsurface phonons,” *Proceedings of the Royal Society A*, vol. 471, p. 20140928, 2015.
- [24] Installation of a PSub may be effectively concealed because it is placed underneath the surface. In other words, an external observer viewing a PSub-installed airplane wing would view a normally looking surface and would not be able to identify if a PSub is present or not.
- [25] C. J. Barnes, C. L. Willey, K. Rosenberg, A. Medina, and A. T. Juhl, “Initial computational investigation toward passive transition delay using a phononic subsurface,” in *AIAA Scitech 2021 Forum*, p. 1454, 2021.
- [26] A. Kianfar and M. I. Hussein, “Phononic-subsurface flow stabilization by subwavelength locally resonant metamaterials,” *New Journal of Physics*, vol. 25, no. 5, p. 053021, 2023.
- [27] C. Willey, C. Barnes, V. Chen, K. Rosenberg, A. Medina, and A. T. Juhl, “Tollmien–schlichting wave manipulation by a multi-input multi-output phononic subsurface,” *The Journal of the Acoustical Society of America*, vol. 155, no. 3-Supplement, pp. A57–A57, 2024.
- [28] R. Schmidt, H. Yousef, I. Roy, C. Scalo, and M. Nouh, “Perturbation energy extraction from a fluid via a subsurface acoustic diode with sustained downstream attenuation,” *Journal of Applied Physics*, vol. 137, no. 5, 2025.
- [29] T. Michelis, A. Putranto, and M. Kotsonis, “Attenuation of tollmien–schlichting waves using resonating surface-embedded phononic crystals,” *Physics of Fluids*, vol. 35, no. 4, p. 044101, 2023.
- [30] A. Kianfar and M. I. Hussein, “Local flow control by phononic subsurfaces over extended spatial domains,” *Journal of Applied Physics*, vol. 134, no. 9, 2023.
- [31] Other lattice symmetries may also be considered in the future.
- [32] W. M. Orr, “The stability or instability of the steady motions of a perfect liquid and of a viscous liquid. part ii: A viscous liquid,” in *Proceedings of the Royal Irish Academy. Section A: Mathematical and Physical Sciences*, vol. 27, pp. 69–138, JSTOR, 1907.
- [33] A. Sommerfeld, *Ein beitrag zur hydrodynamischen erklärung der turbulenten fluessigkeitsbewegungen*. 1909.
- [34] G. Danabasoglu, S. Biringen, and C. L. Streett, “Spatial simulation of instability control by periodic suction blow-

- ing,” *Physics of Fluids A: Fluid Dynamics*, vol. 3, no. 9, pp. 2138–2147, 1991.
- [35] E. M. Saiki, S. Biringen, G. Danabasoglu, and C. L. Streett, “Spatial simulation of secondary instability in plane channel flow: comparison of K- and H-type disturbances,” *Journal of Fluid Mechanics*, vol. 253, p. 485–507, 1993.
- [36] A. Kucala and S. Biringen, “Spatial simulation of channel flow instability and control,” *Journal of Fluid Mechanics*, vol. 738, p. 105–123, 2014.
- [37] M. J. Lighthill, “On displacement thickness,” *Journal of Fluid Mechanics*, vol. 4, pp. 383–392, 1958.
- [38] N. L. Sankar, J. B. Malone, and Y. Tassa, “An implicit conservative algorithm for steady and unsteady three-dimensional transonic potential flows,” in *AIAA Paper 81-1016, June 1981*, 1981.
- [39] M. V. Morkovin, “On roughness—induced transition: facts, views, and speculations,” in *Instability and Transition: Materials of the workshop held May 15-June 9, 1989 in Hampton, Virginia Volume 1*, pp. 281–295, Springer, 1990.
- [40] M. I. Hussein, G. M. Hulbert, and R. A. Scott, “Dispersive elastodynamics of 1d banded materials and structures: analysis,” *Journal of Sound and Vibration*, vol. 289, no. 4-5, pp. 779–806, 2006.
- [41] N. M. Newmark, “A method of computation for structural dynamics,” *Journal of the Engineering Mechanics Division*, vol. 85, no. 3, pp. 67–94, 1959.
- [42] C. Farhat and M. Lesoinne, “Two efficient staggered algorithms for the serial and parallel solution of three-dimensional nonlinear transient aeroelastic problems,” *Computer Methods in Applied Mechanics and Engineering*, vol. 182, pp. 499–515, 2000.

SUPPLEMENTARY MATERIAL

Scatterless interferences: Delay of laminar-to-turbulent flow transition by a lattice of subsurface phonons

Mahmoud I. Hussein*

*Smead Department of Aerospace Engineering Sciences,
University of Colorado, Boulder, Colorado 80303 and
Department of Physics, University of Colorado, Boulder, Colorado 80302*

David Roca

*Centre Internacional de Mètodes Numèrics en Enginyeria (CIMNE),
Universitat Politècnica de Catalunya, Barcelona 08034, Spain*

Adam R. Harris and Armin Kianfar

*Smead Department of Aerospace Engineering Sciences,
University of Colorado, Boulder, Colorado 80303*

This Supplementary Material document covers the application of Bloch's theorem [S1, S2] for two contrasting problems. The first is the acoustic wave propagation problem where acoustic pressure waves experience interferences by a lattice of elastic pillars placed above the surface (Section S1). The second is the flow fluctuation wave propagation problem where flow fluctuation waves experience interferences by a lattice of phononic subsurface (PSub) units (Section S2).

S1. BLOCH ANALYSIS OF ACOUSTIC WAVES SCATTERED BY LATTICE OF ELASTIC PILLARS: LATTICE PLACED ABOVE THE SURFACE

First we analyze the propagation of acoustic pressure waves through a lattice of elastic scatterers. This is a widely studied problem [S3], but provides a contrast to our PSub-flow interaction problem which we cover below. Here the scatterers are in the same spatial domain as the waves being scattered, i.e., above the surface. We consider squared and hexagonal lattice configurations of elastic pillars. More specifically, the scatterers are modelled as infinite pillars in the vertical direction with a squared cross-section of size b and periodically distributed with a center-to-center distance a . The values of a and b , as well as the material properties of these scatterers, have been taken as those for the PSub in the flow problem. The same fluid properties have been considered for the acoustic domain, i.e., the space between the scatterers. The coupled elastoacoustic problem has been solved for a 2D horizontal slice in the frequency domain using COMSOL. The model ensures compatibility at the acoustic-solid interfaces by imposing

$$\omega^2 \mathbf{u} \cdot \mathbf{n} = \partial_n p, \quad (\text{S1})$$

$$\mathbf{f} = -p\mathbf{n}, \quad (\text{S2})$$

where \mathbf{n} is the outward normal vector at the solid boundaries, \mathbf{u} and \mathbf{f} denote the displacement field and external force's amplitudes in the solid domain, and p refers to the acoustic pressure's amplitude.

To obtain the band structure characteristics, a dispersion analysis has been performed on a unit cell imposing Bloch boundary conditions at its edges, namely

$$p(\mathbf{x} + \mathbf{a}) = p(\mathbf{x})e^{i\boldsymbol{\kappa} \cdot \mathbf{a}}, \quad (\text{S3})$$

where \mathbf{a} is the periodicity vector and $\boldsymbol{\kappa}$ is the wavevector. The results are given in Fig. S1 and reveal the presence of a several Bragg scattering bandgaps for acoustic transmission in the streamwise x -direction (Γ -X portion in the squared lattice case, and Γ -M section in the hexagonal lattice case). To better appreciate the effects of these bandgaps, and on the scattering mechanisms that lead to the acoustic wave's amplitude attenuation, a second analysis has been performed in a truncated configuration to 3 unit cells in the streamwise direction. In this study, Bloch boundary conditions are still applied on the top and bottom boundaries of the acoustic domain. On the left (upstream) edge of

* mih@colorado.edu

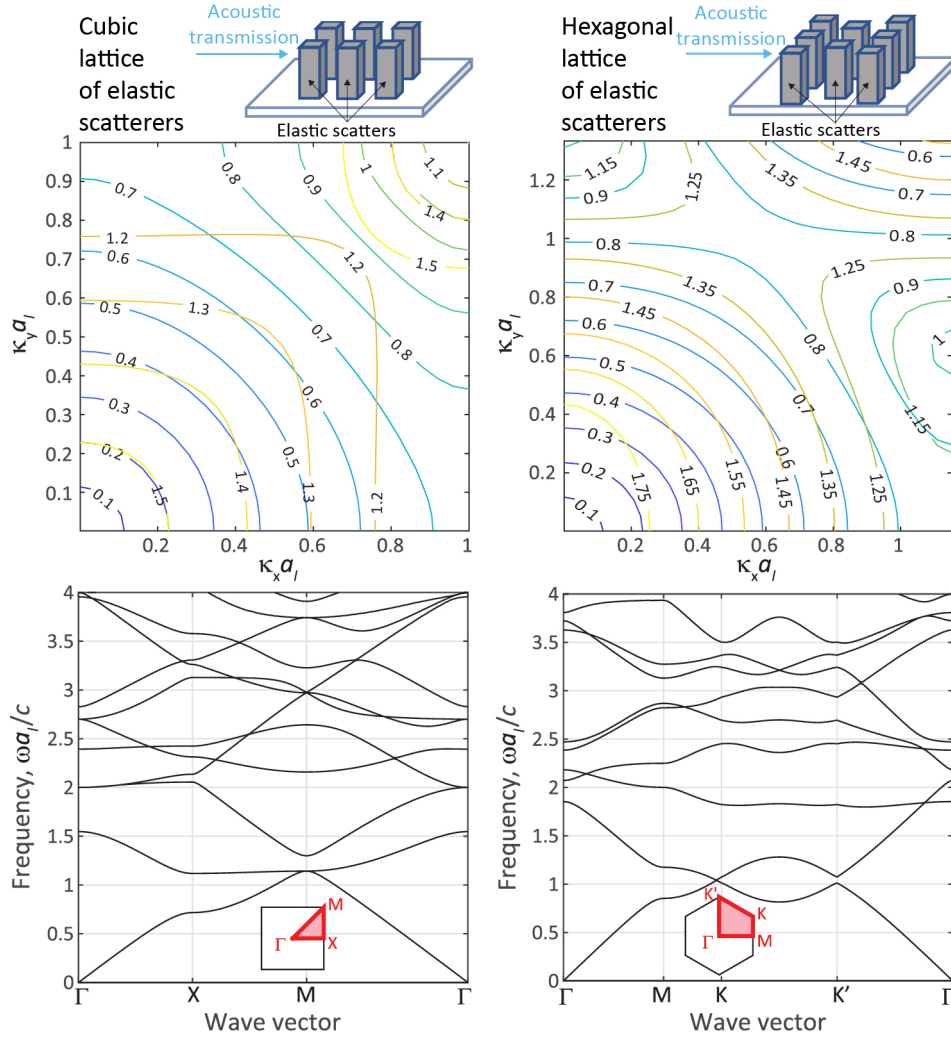


Figure S1. Top row shows a schematic representation of the elastoacoustic problem of an acoustic wave travelling through a periodic lattice of elastic scatterers in the form of infinitely long pillars arranged in squared (left) and hexagonal (right) configurations. The middle and bottom plots show the isofrequency contours and band structure diagrams, respectively, obtained for each case. The irreducible Brillouin zones in the reciprocal space are depicted in the insets at the bottom.

the domain, an incident pressure plane wave travelling in the streamwise direction is imposed. A perfectly matched layer is imposed on the right edge at a far enough downstream distance from the scatterers, to model the infinite extension of the domain. The results for this analysis at a frequency lying inside the first bandgap for both the squared and hexagonal lattices are found in Fig. 4 in the main article.

S2. BLOCH ANALYSIS OF FLOW FLUCTUATION WAVES INFLUENCED BY LATTICE OF PHONONIC SUBSURFACE UNITS: LATTICE PLACED BENEATH THE SURFACE

Now we examine our main problem, namely, undergoing Bloch analysis of the flow fluctuations (instability waves) traveling in a channel where the bottom wall includes a lattice of PSubs in the subsurface. This problem is set up as a stability analysis of the Navier-Stokes equations applied to a channel flow with a given Reynolds number,

$$\text{Re} = \frac{\rho_f U_c \delta}{\mu_f}, \quad (\text{S4})$$

where ρ_f and μ_f are the fluid's density and viscosity, U_c is the flow speed at the centre of the channel (considered the reference velocity) and δ is half the channel's height (used as reference length). A Tollmien-Schlichting (TS)

perturbation is assumed to propagate along the flow, characterized by a frequency ω_{TS} and a wavelength $\lambda_{\text{TS}} = 2\pi\delta$.

On the bottom wall, a lattice of PSub structures are distributed along the xz -plane. For the purpose of this analysis, the interfaces between the PSubs and the flow are modeled as squared units/patches with side length $b = \lambda_{\text{TS}}/4$. These units are arranged in a squared or a hexagonal lattice, with a centre-to-centre distance $a = \lambda_{\text{TS}}/2$. In the forthcoming analysis, the same data used in the main article has been considered, including the Reynolds number $\text{Re} = 7500$ and the parameters $\delta = 4.38 \times 10^{-4}$ m, $\rho_f = 1000$ kg/m³ and $\mu_f = 10^{-3}$ Pa.s.

A. Modelling the PSub response

The PSub structure is assumed to have a one-dimensional response in the y -direction normal to the wall. This response is modelled in terms of an axial displacement η driven by the governing equations of an elastic slender rod structure. In matrix form, the FE-discretized system of equations yields

$$[\mathbf{M}]\{\ddot{\eta}\} + [\mathbf{C}]\{\dot{\eta}\} + [\mathbf{K}]\{\eta\} = \{\mathbf{f}\}, \quad (\text{S5})$$

where $[\mathbf{M}]$ is the mass matrix, $[\mathbf{K}]$ is the stiffness matrix, and $[\mathbf{C}]$ is the damping matrix. The system is excited at the interface with the flow by the perturbation pressure from the fluid, so $f(0, t) = -p_w(t)$ (the negative sign indicates that the force acts opposite to the outward normal to the wall), and at the other end the displacement is fixed $\eta(-L, t) = 0$. The sub-index 'w' is used to denote the PSub-flow interface, i.e., $y = 0$. Given the one-dimensional nature of the system, everything is normalized by the the PSub patch surface area.

Assuming harmonic excitation at a given frequency ω ,

$$p_w(t) = \bar{p}_w e^{-i\omega t} + c.c., \quad (\text{S6})$$

the system in (S5) can be solved to find the amplitude of the displacement at the flow interface, $\bar{\eta}_w$. This allows us to define the admittance of the PSub as

$$Y_{\text{PSub}} = \frac{\dot{\eta}_w}{p_w} \rightarrow \bar{Y}_{\text{PSub}} = \frac{-i\omega\bar{\eta}_w}{\bar{p}_w}. \quad (\text{S7})$$

It is worth noting that \bar{Y}_{PSub} can be obtained, for a given frequency, by solving the system in (S5) in the frequency domain with $\bar{p}_w = 1$. From (S7), it can be seen that the product between the amplitude and the phase of \bar{Y}_{PSub} is proportional to the performance metric used to characterize the PSub.

B. Model of a unit cell in the PSub-influenced fluid domain

In what follows, partial derivatives will be denoted by $\partial_\phi(\bullet) = \partial(\bullet)/\partial\phi$. In this regard, the gradient operator will be defined as $\nabla = (\partial_x, \partial_y, \partial_z)$ and the Laplacian operator $\Delta = \partial_x^2 + \partial_y^2 + \partial_z^2$. Starting with the three-dimensional Navier-Stokes equations,

$$\nabla \cdot \mathbf{V} = 0, \quad (\text{S8})$$

$$\partial_t \mathbf{V} + (\mathbf{V} \cdot \nabla) \mathbf{V} + \nabla P - \frac{1}{\text{Re}} \Delta \mathbf{V} = \mathbf{0}. \quad (\text{S9})$$

where $\mathbf{V} = (U, V, W)$ are the fluid velocity components, and P refers to the pressure field. We will assume the velocity and pressure fields can be decomposed into the base flow components, \mathbf{v}_b and p_b , and *small* perturbation components, $\mathbf{v} = (u, v, w)$ and p , such that

$$\mathbf{V} = \mathbf{v}_b + \mathbf{v}, \quad (\text{S10})$$

$$P = p_b + p. \quad (\text{S11})$$

The base flow components are assumed to satisfy (S8) and (S9) for an incompressible parallel flow in the x -direction (channel flow), hence $\mathbf{v}_b = (u_b(y), 0, 0)$, with

$$u_b = 1 - (1 - y)^2, \quad u'_b = 2(1 - y), \quad u''_b = -2. \quad (\text{S12})$$

Substituting (S10) and (S11) into (S8) and (S9) and neglecting second order terms we get

$$\partial_x u + \partial_y v + \partial_z w = 0, \quad (\text{S13})$$

and

$$\partial_t u + u_b \partial_x u + u'_b v + \partial_x p - \frac{1}{\text{Re}} \Delta u = 0, \quad (\text{S14a})$$

$$\partial_t v + u_b \partial_x v + \partial_y p - \frac{1}{\text{Re}} \Delta v = 0, \quad (\text{S14b})$$

$$\partial_t w + u_b \partial_x w + \partial_z p - \frac{1}{\text{Re}} \Delta w = 0. \quad (\text{S14c})$$

To eliminate of the pressure, first, we take the divergence of (S14), which yields

$$\Delta p = -2u'_b \partial_x v. \quad (\text{S15})$$

An alternative pressure equation, which will be convenient in the forthcoming derivations, can be obtained by subtracting the partial derivative ∂_y of (S14b) from (S15),

$$(\partial_x^2 + \partial_z^2)p = \left(\partial_t \partial_y + (u_b \partial_y - u'_b) \partial_x - \frac{1}{\text{Re}} \partial_y \Delta \right) v. \quad (\text{S16})$$

Then, by taking the Laplacian of (S14b) and substituting (S15), we get

$$\left((\partial_t + u_b \partial_x) \Delta - u''_b \partial_x - \frac{1}{\text{Re}} \Delta^2 \right) v = 0, \quad (\text{S17})$$

where $\Delta^2 = \partial_x^4 + \partial_y^4 + \partial_z^4 + 2(\partial_y^2 \partial_z^2 + \partial_z^2 \partial_x^2 + \partial_x^2 \partial_y^2)$. It is worth noting that once v is obtained from (S17), then either (S16) or (S15) can be solved to get the pressure field. Once p and v are known, the u and w components of the perturbation velocity field can be obtained from (S14a) and (S14c), respectively.

To deal with the temporal term in the partial differential equations, the system will be expressed in the frequency domain, hence

$$\mathbf{v}(\mathbf{x}, t) = \bar{\mathbf{v}}(\mathbf{x}) e^{-i\omega t} + c.c., \quad (\text{S18})$$

$$p(\mathbf{x}, t) = \bar{p}(\mathbf{x}) e^{-i\omega t} + c.c. \quad (\text{S19})$$

Furthermore, assuming the perturbation propagates in the x -direction,

$$\bar{\mathbf{v}}(\mathbf{x}) = \tilde{\mathbf{v}}(\mathbf{x}) e^{i\kappa x}, \quad (\text{S20})$$

$$\bar{p}(\mathbf{x}) = \tilde{p}(\mathbf{x}) e^{i\kappa x}. \quad (\text{S21})$$

where κ refers to the wavenumber of the T-S perturbation. The combination of Eqs. (S18)-(S21) renders a plane wave solution.

Thus far, the formulation follows the standard Orr-Sommerfeld approach [S4–S6]. Now we account for the periodic arrangement of the PSubs in the xz -plane, and apply Bloch's theorem [S1, S2] to a single unit cell representing the flow domain over a single PSub with the fluid-structure interaction accounted for. It follows that the amplitude fields $\tilde{\mathbf{v}}$ and \tilde{p} must be periodic in the xz spatial domain. To impose the periodicity required by Bloch's theorem, a two-dimensional Fourier expansion is considered, hence

$$\tilde{\mathbf{v}}(\mathbf{x}) = \sum_n \hat{\mathbf{v}}_n(y) e^{i(\alpha_n x + \beta_n z)}, \quad (\text{S22})$$

$$\tilde{p}(\mathbf{x}) = \sum_n \hat{p}_n(y) e^{i(\alpha_n x + \beta_n z)}, \quad (\text{S23})$$

where $\hat{\mathbf{v}}_n$ and \hat{p}_n are the amplitude coefficients associated to the n -th component in the series, and α_n and β_n are the corresponding Fourier wavenumbers. In general, for a truncated series with $2N_x + 1$ and $2N_z + 1$ terms in each direction, each n -th component in the summation will be associated with a pair of indices $(i, j)_n$ in the ranges $i = \{-N_x, \dots, 0, \dots, N_x\}$ and $j = \{-N_z, \dots, 0, \dots, N_z\}$. In this regard, we have

$$\alpha_n = \begin{cases} i_n \frac{2\pi}{a}, & \text{for the squared lattice,} \\ \frac{2i_n - j_n}{\sqrt{3}} \frac{2\pi}{a}, & \text{for the hexagonal lattice,} \end{cases} \quad \text{and} \quad \beta_n = j_n \frac{2\pi}{a}. \quad (\text{S24})$$

With these definitions, we can deal with the partial derivatives $\partial_t \equiv -i\omega$, $\partial_x \equiv i(\kappa + \alpha_n)$ and $\partial_z \equiv i\beta_n$. Then, substituting into (S17), we get a fourth-order ordinary differential equation for each n component in the series expansion, in terms of the Fourier amplitude \hat{v}_n (which is only a function of the spatial y -coordinate),

$$\left((\omega - u_b(\kappa + \alpha_n))\Delta + u_b''(\kappa + \alpha_n) + \frac{i}{\text{Re}}\Delta^2 \right) \hat{v}_n = 0, \quad (\text{S25})$$

where $\Delta = \partial_y^2 - ((\kappa + \alpha_n)^2 + \beta_n^2)$ and $\Delta^2 = \partial_y^4 - 2((\kappa + \alpha_n)^2 + \beta_n^2)\partial_y^2 + ((\kappa + \alpha_n)^2 + \beta_n^2)^2$. It is worth noting that (S25) is the generalized Orr-Sommerfeld equation to a three-dimensional spatial domain. In fact, one recovers the classical one-dimensional version by making $\alpha_n = \beta_n = 0$.

To account for the PSub interaction with the flow, no-slip transpiration boundary conditions are applied [S7]. For the case of a moving wall with small displacements in the normal y -direction, these take the form of

$$u(x, 0, z, t) = -u_b'(0)\eta_w\mathcal{H}(x, z), \quad (\text{S26a})$$

$$v(x, 0, z, t) = \dot{\eta}_w\mathcal{H}(x, z), \quad (\text{S26b})$$

$$w(x, 0, z, t) = 0, \quad (\text{S26c})$$

where $\tilde{\eta}_w$ refers to the PSub displacement, and \mathcal{H} is a periodic step function defined such that $\mathcal{H} = 1$ for $(x, z) \in \Gamma_{\text{PSub}}$ (i.e., in the area occupied by the PSub patches) and $\mathcal{H} = 0$ otherwise. Expressing (S26) in the frequency domain and using the definition in (S7), we get

$$i\omega\tilde{u}(x, 0, z) = u_b'(0)\bar{Y}_{\text{PSub}}\tilde{p}_w\mathcal{H}(x, z), \quad (\text{S27a})$$

$$\tilde{v}(x, 0, z) = \bar{Y}_{\text{PSub}}\tilde{p}_w\mathcal{H}(x, z), \quad (\text{S27b})$$

$$\tilde{w}(x, 0, z) = 0. \quad (\text{S27c})$$

It is worth noting that the TS wave spatial perturbation component has also been accounted for in (S27), assuming $\tilde{p}_w = \tilde{p}_w e^{i\kappa x}$. To proceed, the two-dimensional Fourier expansion is applied, yielding

$$i\omega\hat{u}_n(0) = u_b'(0)\bar{Y}_{\text{PSub}}\tilde{p}_w\hat{\mathcal{H}}_n, \quad (\text{S28a})$$

$$\hat{v}_n(0) = \bar{Y}_{\text{PSub}}\tilde{p}_w\hat{\mathcal{H}}_n, \quad (\text{S28b})$$

$$\hat{w}_n(0) = 0, \quad (\text{S28c})$$

where $\hat{\mathcal{H}}_n$ are the Fourier coefficients for the step function, given by

$$\hat{\mathcal{H}}_n = \frac{1}{a^2} \int_{-b/2}^{b/2} \int_{-b/2}^{b/2} e^{i(\alpha_n x + \beta_n z)} dx dz = \frac{\sin(\alpha_n b/2)}{\alpha_n a/2} \frac{\sin(\beta_n b/2)}{\beta_n a/2}. \quad (\text{S29})$$

Using (S13), the boundary condition (S28a) can be re-written as

$$\omega\partial_y\hat{v}_n(0) = -(\kappa + \alpha_n)u_b'(0)\hat{v}_n(0). \quad (\text{S30})$$

To make the analysis consistent with the FSI simulations, the pressure amplitude value that triggers the PSub response is taken as the average over Γ_{PSub} , hence

$$\tilde{p}_w = \frac{1}{b^2} \int_{-b/2}^{b/2} \int_{-b/2}^{b/2} \tilde{p}(x, 0, z) dx dz = \frac{a^2}{b^2} \sum_m \hat{p}_m(0)\hat{\mathcal{H}}_m. \quad (\text{S31})$$

Equation (S16) can be used to express the pressure coefficients at the wall in terms of the vertical component of the perturbation velocity, such that

$$\hat{p}_m(0) = \frac{1}{((\kappa + \alpha_m)^2 + \beta_m^2)\text{Re}} (\partial_y^3 - ((\kappa + \alpha_m)^2 + \beta_m^2)\partial_y) \hat{v}_m(0). \quad (\text{S32})$$

Then, the boundary condition (S28b) can be expressed as

$$\hat{v}_n(0) = \frac{\bar{Y}_{\text{PSub}} a^2}{\text{Re} b^2} \sum_m \left(\frac{\hat{\mathcal{H}}_m \hat{\mathcal{H}}_n}{(\kappa + \alpha_m)^2 + \beta_m^2} (\partial_y^3 - ((\kappa + \alpha_m)^2 + \beta_m^2)\partial_y) \hat{v}_m(0) \right). \quad (\text{S33})$$

The introduction of the PSub admittance as a boundary condition has been used in Ref. [S8] in the context of a similar stability analysis but considering only a lone PSub occupying the entire boundary layer, as opposed to a lattice of PSubs.

Noticeably, by setting $\bar{Y}_{\text{PSub}} = 0$, the conventional rigid wall boundary conditions are recovered. These are applied on the top wall as

$$\hat{v}_n(2) = 0, \quad (\text{S34})$$

$$\partial_y \hat{v}_n(2) = 0. \quad (\text{S35})$$

The whole set of (S25), with the corresponding boundary conditions provided by (S31) and (S33) for the bottom wall and by (S34) and (S35) for the top wall, represent a system that can be solved for a given frequency ω and the associated PSub admittance \bar{Y}_{PSub} as a generalized eigenvalue problem, in which the wavenumber κ becomes the eigenvalue and each \hat{v}_n represents an eigenfunction. It is worth noting that in order for κ to represent the eigenvalue, first (S33) must be multiplied by the common denominator, which increases the order of the generalized eigenvalue problem. Regardless, a solution can be found numerically upon applying some form of spatial discretization of the terms \hat{v}_n . In this work, a finite-element based scheme with standard Hermite elements—to capture the higher-order derivatives involved—is considered.

For each eigenvalue κ , from the associated eigenfunctions \hat{v}_n —or eigenvectors, in the discretized version of the problem—one can obtain the corresponding pressure coefficients \hat{p}_n from (S15) or (S16). Then, the remaining perturbation velocity components \hat{u}_n and \hat{w}_n can be obtained from (S14a) and (S14c), respectively. Alternatively, (S13) can be used once either \hat{u}_n or \hat{w}_n has been obtained to find the other.

Bloch’s theorem has been widely used for acoustic and elastic wave propagation problems, as demonstrated in Section S1. The theorem has recently also been applied to a flow stability problem involving a repeated one-dimensional array of rigid riblets in a channel [S9]. In that work, the analysis domain comprised several repeated cells, and the focus has been on calculating the complex frequency response for a given wavenumber. Here, we examine a two-dimensional lattice of PSubs placed in the subsurface, with the fluid-structure interaction accounted for, and considering both square and hexagonal symmetries. We also limit our analysis to a single unit cell, as commonly done in Bloch analysis. Furthermore, we calculate the flow perturbations dispersion curves for the most unstable mode. In the main article, we discuss, and demonstrate, the benefit of this analysis on guiding the PSub lattice design to achieve delay of flow transition.

C. Energetics of the Bloch solution

To focus the stability analysis on the most relevant mode, we select the closest to the unstable mode resulting from the classical Orr-Sommerfeld equation, which has been used as input of the T-S wave in the FSI simulations. In our framework, this can be obtained simply by setting $\bar{Y}_{\text{PSub}} = 0$ on the bottom wall boundary conditions. Tracking this mode for a selected range of frequencies allows us to obtain the stability plots given in Figure S3(a). The results show a correlation between the real and imaginary components of the admittance with the imaginary and real components of the unstable wavenumber, respectively. As the value of the admittance increases, the PSub effects are more noticeable, consistently with what the PSub performance metric indicates. Incidentally, in order to visualize the destabilizing and stabilizing effects, we evaluate the rate of production of perturbation kinetic energy (PKE) density for the associated mode. To do so, once the corresponding \hat{v}_n and \hat{u}_n terms have been obtained, (S22) is used to get the complex amplitude of the mode at a given point, which can be expressed in terms of its absolute value $|\tilde{\mathbf{v}}(\mathbf{x})|$ and phase $\varphi_{\tilde{\mathbf{v}}}(\mathbf{x})$ as

$$\tilde{u}(\mathbf{x}) = |\tilde{u}(\mathbf{x})|e^{i\varphi_{\tilde{u}}(\mathbf{x})}, \quad (\text{S36a})$$

$$\tilde{v}(\mathbf{x}) = |\tilde{v}(\mathbf{x})|e^{i\varphi_{\tilde{v}}(\mathbf{x})}, \quad (\text{S36b})$$

$$\tilde{w}(\mathbf{x}) = |\tilde{w}(\mathbf{x})|e^{i\varphi_{\tilde{w}}(\mathbf{x})}. \quad (\text{S36c})$$

The T-S wave propagation can then be defined using (S18) as

$$u(\mathbf{x}, t) = 2|\tilde{u}(\mathbf{x})|e^{-\kappa_1 x} \cos(\kappa_R x - \omega t + \varphi_{\tilde{u}}(\mathbf{x})), \quad (\text{S37a})$$

$$v(\mathbf{x}, t) = 2|\tilde{v}(\mathbf{x})|e^{-\kappa_1 x} \cos(\kappa_R x - \omega t + \varphi_{\tilde{v}}(\mathbf{x})), \quad (\text{S37b})$$

$$w(\mathbf{x}, t) = 2|\tilde{w}(\mathbf{x})|e^{-\kappa_1 x} \cos(\kappa_R x - \omega t + \varphi_{\tilde{w}}(\mathbf{x})), \quad (\text{S37c})$$

where $\kappa = \kappa_R + i\kappa_I$ has been considered. Then, the average modal PKE density over one period of time $T = 2\pi/\omega$ is obtained as

$$k(\mathbf{x}) = \frac{1}{T} \int_0^T \frac{1}{2} \left([u(\mathbf{x}, t)]^2 + [v(\mathbf{x}, t)]^2 + [w(\mathbf{x}, t)]^2 \right) dt = (|\tilde{u}(\mathbf{x})|^2 + |\tilde{v}(\mathbf{x})|^2 + |\tilde{w}(\mathbf{x})|^2) e^{-2\kappa_I x}. \quad (\text{S38})$$

In a similar fashion, the average rate of production of modal PKE density is computed as

$$p_r(\mathbf{x}) = -\frac{1}{T} \int_0^T u(\mathbf{x}, t)v(\mathbf{x}, t)u'_b dt = -2|\tilde{u}(\mathbf{x})||\tilde{v}(\mathbf{x})|u'_b e^{-2\kappa_I x} \cos(\varphi_{\tilde{u}}(\mathbf{x}) - \varphi_{\tilde{v}}(\mathbf{x})). \quad (\text{S39})$$

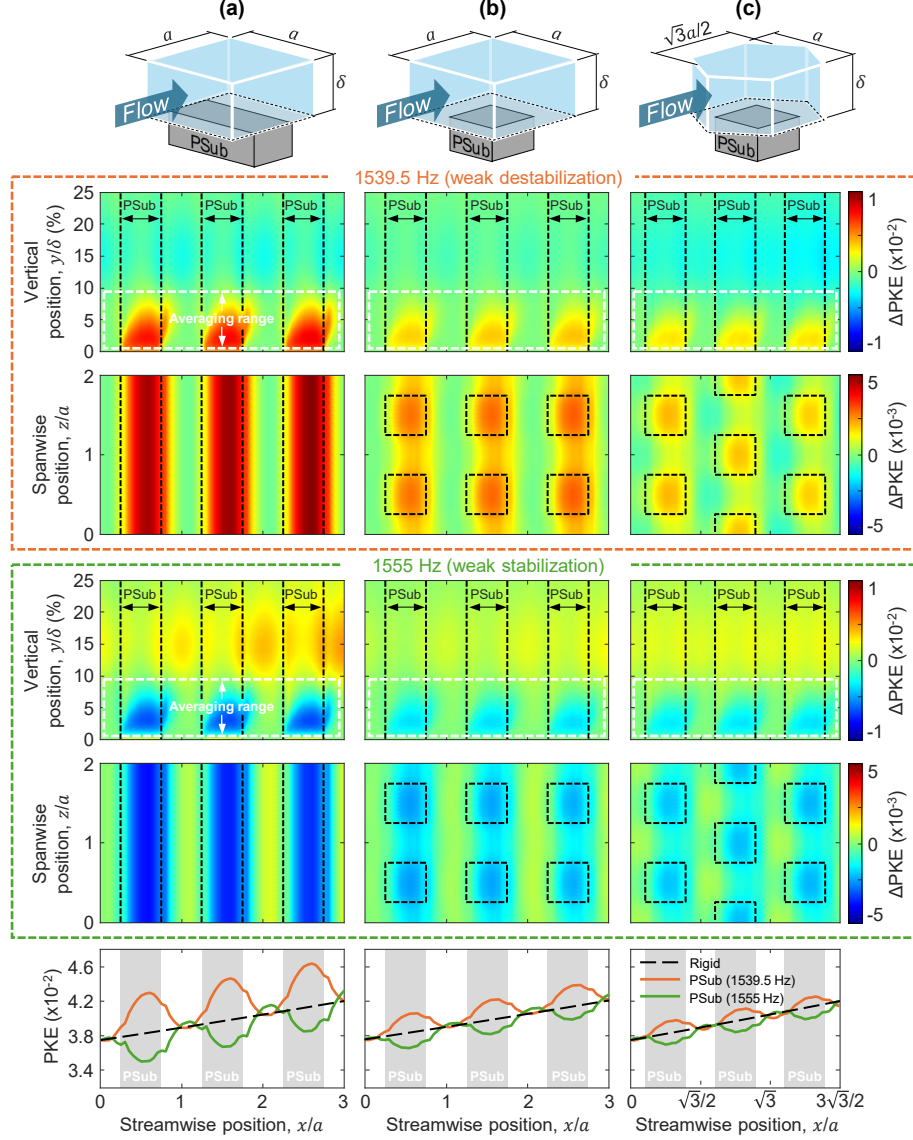


Figure S2. Perturbation kinetic energy (PKE) distributions corresponding to the unstable mode for the (a) full-span, (b) square lattice, and (c) hexagonal lattice configurations depicted in the top row. Results for each frequency are depicted in their corresponding panel. The first panel (in orange) shows a weak destabilizing case (at a frequency of 1539.5 Hz) and the second panel (in light green) is for a weak stabilizing case (at a frequency of 1555 Hz). In each panel, the top row depicts the average (over the entire spanwise direction) vertical distribution of the modal PKE difference between the PSub case and the rigid case, denoted ΔPKE , while the bottom row shows the horizontal distribution of the same property, averaged in the vicinity of the PSub wall (where the effect is stronger), up to 10% of half of the channel's height (see region highlighted in white in the vertical distribution plots). The bottom plots below the panels summarize the averaged modal PKE evolution obtained for both the weak destabilizing and stabilizing cases compared to that of the rigid case. As a reference, all the modal amplitudes have been normalized to make them coincide with that of the rigid case at the left edge of the first unit cell.

From equation (S39), it can be seen that the sign of the production rate is determined by the relative phase between the horizontal and vertical components of the perturbation velocity, being positive when they are in-phase, and negative when they are out-of-phase.

To show the consistency of this analysis with the predicted effects of the PSub by the performance metric, Fig. S2 shows the computed PKE obtained from the perturbation velocity components of the unstable mode for the different PSub configurations (full-span, square lattice, and hexagonal lattice). Two frequencies have been selected for the analysis, one at 1539.5 Hz—corresponding to a destabilizing case—and another at 1555 Hz—corresponding to a stabilizing case. To better visualize the effects, the modal amplitudes in each case have been normalized so that the average PKE at the left edge of the first unit cell is the same as in the rigid case. Using the latter as reference, the results in Fig. S2 clearly show how in the destabilizing case the modal PKE increases close to the wall in the sections where the flow interacts with the PSub, with the effects being stronger in the full-span case compared to the lattice configurations. Conversely, for the stabilizing frequency, the modal PKE is reduced instead.

These results are also consistent with the stability plots shown in Fig. S3(a) where the same results are compared with those obtained at frequencies with stronger PSub interaction effects, namely at 1545 Hz and 1549.4 Hz for the strong destabilization and stabilization cases, respectively. From Fig. S3 it can be seen that the absolute value of the admittance is higher at these frequencies, which translates into larger real and imaginary wavenumbers corresponding to the unstable mode. Consistently, both the modal PKE and the associated production rates exhibit much higher amplitudes for these cases [see Fig. S3(b)-(d)]. One can also observe how, for the same PSub admittance, the full-span configuration yields a much stronger response than the lattice cases, both in terms of the modal amplitudes of the PKE and the associated imaginary wavenumber component κ_I . This can be attributed to interaction effects in the spanwise direction which have the potential to alter the flow instabilities downstream, as demonstrated in the full-scale FSI simulations of the truncated lattices.

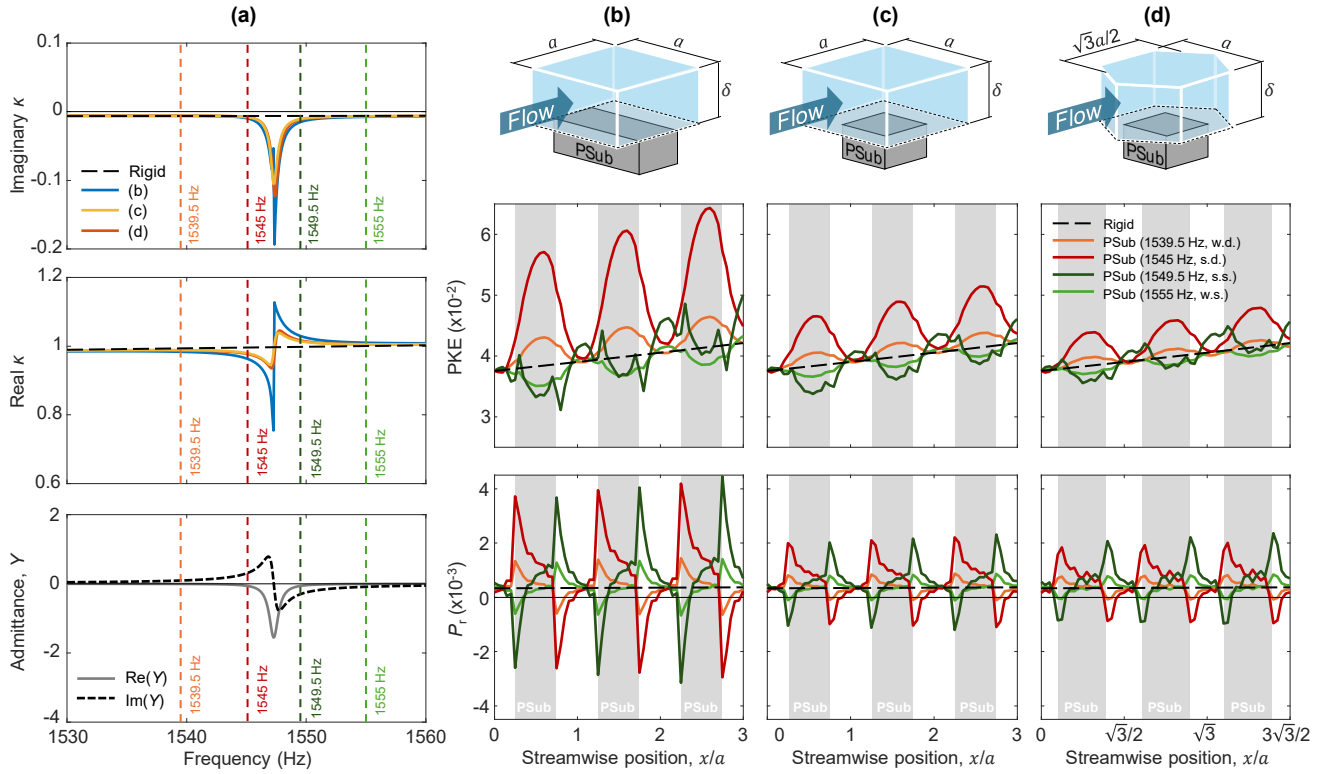


Figure S3. (a) Dispersion curves corresponding to the unstable mode. The first and second rows correspond to the imaginary and real components of the wavenumber κ for the rigid cases and the PSub cases in the full-span, square lattice, and hexagonal lattice configurations [depicted by the (b), (c) and (d) unit cell schematics, respectively]. The third row shows the real and imaginary components of the PSub's admittance Y at different frequencies. The dashed vertical lines indicate the frequencies for which the average modal perturbation kinetic energy (PKE) and their corresponding rates of production P_r curves on the right plots have been obtained. In particular, weak and strong destabilizing (in orange and dark red, respectively) and weak and strong stabilizing (in light and dark green, respectively) have been considered. The PKE and production rate curves correspond to averages over the entire spanwise direction and the first 10% section of half of the channel's height in the vicinity of the PSub wall (as in Fig. S2). The modal amplitudes have been normalized to make them coincide with that of the rigid case at the left edge of the first unit cell in each case.

-
- S1 F. Bloch, Über die quantenmechanik der elektronen in kristallgittern, *Z. Phys.* **52**, 555 (1929).
- S2 M. I. Hussein, M. J. Leamy, and M. Ruzzene, Dynamics of phononic materials and structures: Historical origins, recent progress, and future outlook, *Applied Mechanics Reviews* **66** (2014).
- S3 M. Sigalas and E. Economou, Attenuation of multiple-scattered sound, *Europhysics Letters* **36**, 241 (1996).
- S4 W. M. Orr, The stability or instability of the steady motions of a perfect liquid and of a viscous liquid. part ii: A viscous liquid, in *Proceedings of the Royal Irish Academy. Section A: Mathematical and Physical Sciences*, Vol. 27 (JSTOR, 1907) pp. 69–138.
- S5 A. Sommerfeld, *Ein beitrug zur hydrodynamischen erklärung der turbulenten fluessigkeitsbewegungen* (1909).
- S6 T. B. Benjamin, Effects of a flexible boundary on hydrodynamic instability, *Journal of Fluid Mechanics* **9**, 513 (1960).
- S7 A. Kianfar and M. I. Hussein, Phononic-subsurface flow stabilization by subwavelength locally resonant metamaterials, *New Journal of Physics* **25**, 053021 (2023).
- S8 C. J. Barnes, C. L. Willey, K. Rosenberg, A. Medina, and A. T. Juhl, Initial computational investigation toward passive transition delay using a phononic subsurface, in *AIAA Scitech 2021 Forum* (2021) p. 1454.
- S9 A. Jouin, J.-C. Robinet, and S. Cherubini, Modal and nonmodal stability of the laminar flow in a channel with longitudinal riblets, *Physical Review Fluids* **9**, 073903 (2024).